ACS APPLIED MATERIALS & INTERFACES
Research Article
Cite This: ACS Appl. Mater. Interfaces 2019, 11, 39376−39384
www.acsami.org

L-Histidine Crystals as Efficient Vehicles to Deliver Hydrophobic Molecules

Raheleh Ravanfar and Alireza Abbaspourrad*

Department of Food Science, Cornell University, Ithaca, New York 14853, United States

Supporting Information

ABSTRACT: L-Histidine (L-His) molecules can form highly ordered fluorescent crystals with tunable size and geometry. The polymorph A crystal of L-His contains hydrophobic domains within the structure's interior. Here, we demonstrate that these hydrophobic domains can serve as vehicles for highly efficient entrapment and transport of hydrophobic small molecules. This strategy shows the ability of L-His crystals to mask the hydrophobicity of various small molecules, helping to address issues related to their poor solubility and low bioavailability. Furthermore, we demonstrate that we can modify the surface of these crystals to define their function, suggesting the significance of L-His crystals in designing site-specific and bioresponsive platforms. As a demonstration, we use L-His crystals with loaded doxorubicin, featuring hyaluronic acid covalently bonded on the crystal surface, controlling its release in response to hyaluronidase. This strategy for entrapment of hydrophobic small molecules suggests the potential of L-His crystals for targeted drug-delivery applications.

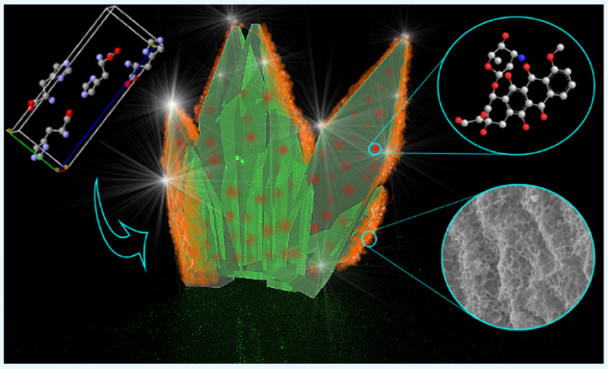

KEYWORDS: *L-histidine, natural fluorescent crystals, drug delivery, hydrophobic small molecules*

■ INTRODUCTION

The clinical use of various potent, hydrophobic molecules is often hampered by their poor water solubility.[1] Low water solubility results in poor absorption as well as low biodistribution and bioavailability of hydrophobic therapeutics upon oral administration.[2] Moreover, low water solubility causes drug aggregation upon intravenous administration, which is associated with local toxicity and lowered systemic bioavailability.[3,4] For example, doxorubicin (DOX) is a widely used hydrophobic anticancer drug with excellent antineoplastic activity against a multitude of human cancers.[5] However, its clinical use is hindered by acute side effects, such as vomiting, bone marrow suppression, and drug-induced irreversible cardiotoxicity.[6] Most of these side effects are due to the poor water solubility of DOX.[7]

These challenges have driven the development of drug-delivery systems to increase the efficacy of hydrophobic therapeutics through improved pharmacokinetics and biodistribution.[8] The drug-delivery systems include particulate lipid- and/or polymer-based carriers and the therapeutics.[4,9,10] The drug-delivery systems can also function as drug reservoirs and improve the pharmacological properties of conventional free drugs.[11−16] A wide variety of scaffolds, such as liposomes[17] and stimuli-responsive polymeric particles,[18,19] have been explored, either covalently or noncovalently conjugating hydrophobic drugs with these systems.[8] Studies have designed the delivery systems using a wide variety of synthetic or natural materials, such as poly-L-lactatide,[20] polyethylene glycol,[21] phosphatidylethanolamine,[22] proteins, and vegetable oils.[23−25] Despite significant advances in the development of such drug carriers, there remain a few problems that have resulted in therapeutic failure, including the lack of site specificity,[26] low biocompatibility,[27] and inefficient drug entrapment within the carriers.[28] Moreover, covalent attachment in some cases requires chemical modification, which can reduce the efficiency of drug release or incomplete intracellular processing of a prodrug compound.[29] These strategies also involve additional complexities associated with mass production difficulties and cost. Thus, the fabrication of biocompatible platforms that can overcome these limitations remains an important yet unmet need.

Previous studies have reported the application of poly(L-histidine) for fabrication of drug delivery systems.[30−32] Here, we demonstrate that L-histidine (L-His) crystals can function as efficient vehicles to entrap hydrophobic free drugs, such as DOX, as well as other hydrophobic small molecules, including Nile red, β-carotene, and pyrene (Figure 1a,b). The noncovalent inclusion of such hydrophobic molecules inside the hydrophobic domains within the interior of the polymorph A crystal structure of L-His suggests the capability for efficient drug transport and release, avoiding prodrug processing issues. As an essential amino acid, L-His crystals also have the

Received: August 9, 2019
Accepted: October 3, 2019
Published: October 3, 2019

DOI: 10.1021/acsami.9b14239

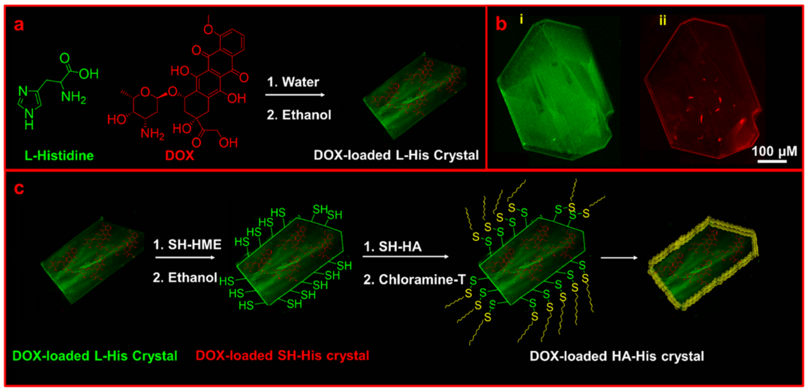

Figure 1. (a) Schematic representation for the preparation of L-His crystals loaded with DOX molecules. (b) CLSM images of (i) L-His crystal emitting green color, (ii) DOX with red color in the L-His crystal. (c) Schematic representation for the preparation of L-His crystals surface-modified with tumor-specific HA for the targeted delivery of hydrophobic DOX molecules.

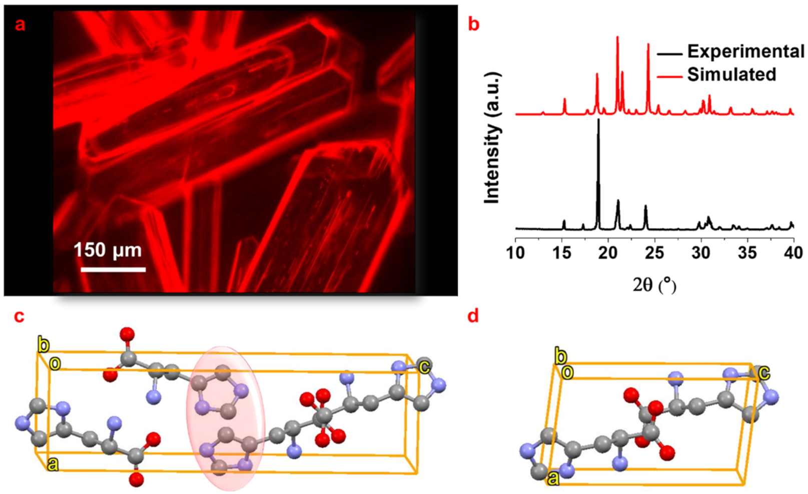

Figure 2. (a) Fluorescence microscopy images of L-His crystals. (b) Simulated and experimental XRD patterns of the pure L-His crystals. (c) Ball and stick representation of four L-His molecules arranged in the polymorph A with the orthorhombic space group $P2_12_12_1$, showing the hydrophobic domain surrounded by imidazole rings of the L-His molecules. (d) Ball and stick representation for the unit cell of crystals formed after loading the small molecules, showing two L-His molecules with monoclinic space group, $P2_1$.

advantage of being biocompatible and feature the ability to load a large quantity of hydrophobic molecules. Furthermore, we have recently discovered the natural fluorescent properties of L-His crystals (the results of which will be reported elsewhere), which suggests their potential as traceable compounds inside biological systems.

In this study, we further demonstrate that L-His crystals can be chemically modified at the surface to provide preferential biological targeting to the desired site of action (Figure 1c). By covalently cross-linking hyaluronic acid (HA) to the surface of L-His crystals (HA-His crystals), we show that hyaluronidase (HAase) is able to hydrolyze the HA on the HA-His crystals, allowing the L-His crystals to dissolve in an aqueous matrix and release encapsulated small molecules, such as DOX, to a desired site. This scaffold provides highly efficient noncovalent inclusion of hydrophobic molecules or active drugs with excellent biocompatibility and efficient bioresponsive drug release. Moreover, the HA-His crystals are potentially site-specific, making them excellent candidates for targeting CD44-receptors overexpressed on tumors, and thus enhancing the permeability of anticancer drugs.

RESULTS AND DISCUSSION

In addition to its well-known role as an electrophilic acid, L-His features two nitrogen atoms, designated as Nδ1 and Nε2, in its heterocyclic imidazole system, which serve as the hydrogen bond acceptor and hydrogen bond donor, respectively.[33−35] To synthesize L-His crystals, we performed antisolvent crystallization, adding ethanol as the antisolvent to an aqueous solution of L-His at a 1:1 volume ratio (Figure 2a). We note that the size of the crystals in length can be tuned from the submicron to micron scale (500 nm to 500 μm), depending on the crystal growth time and antisolvent.[36] The L-His crystals display bright emission at 500 nm (405 nm excitation), which we attribute to suppressed nonradiative decay by intramolecular motion due to the close molecular packing of the crystal (the fluorescence properties of the L-His crystals will be reported elsewhere).

We also investigate the powder X-ray diffraction (XRD) pattern of L-His crystals. The diffraction peaks of the L-His crystal was in good agreement with the simulated diffraction peaks of the crystal from the Cambridge Crystallographic Data Center (CCDC, CIF code 1206541) (Figure 2b). We measured the unit cell data of the resulting pure L-His crystals and found that they were consistent with a previous study of L-

DOI: 10.1021/acsami.9b14239
ACS Appl. Mater. Interfaces 2019, 11, 39376−39384

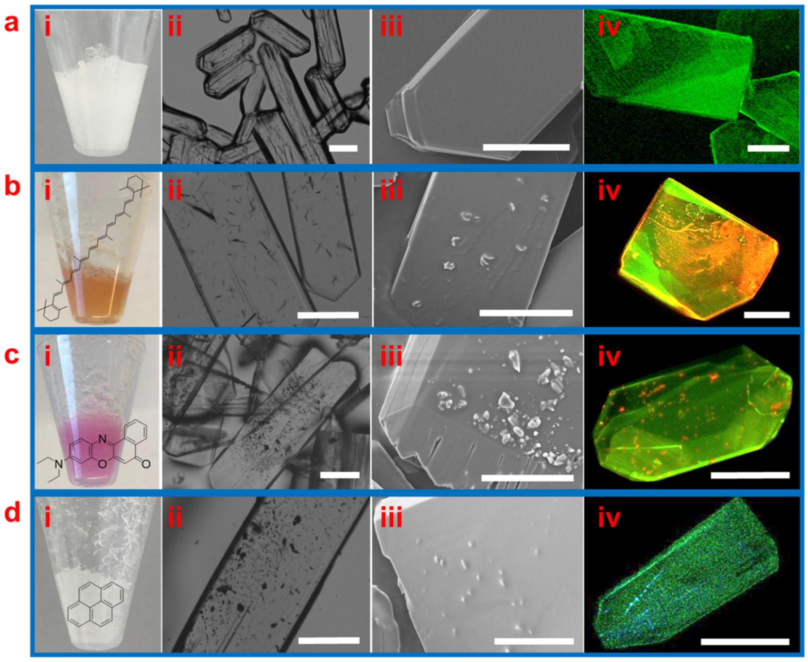

Figure 3. (a) Pure L-His crystals; the green color in part iv represents the pure L-His crystals. (b) β-carotene-entrapped L-His crystals; the green color represents the L-His crystals and the orange color represents β-carotene. (c) Nile red-entrapped L-His crystals; the green color represents the L-His crystals and the red color represents Nile red. (d) Pyrene-entrapped L-His crystals; the green color represents the L-His crystals and the blue color represents pyrene. First column (i) digital images; second column (ii) optical microscopy images; third column (iii) SEM images; fourth column (iv) CLSM images. Scale bars: 100 μm.

His by Madden, et al.[37] (CIF code 1206541) (Figure 2c). X-ray crystallography of our L-His crystals showed a mixture of the stable polymorph A with the orthorhombic space group $P2_12_12_1$ and $Z = 4$ molecules in the unit cell, and the metastable polymorph B with the majority being polymorph A. The relative fractions of these polymorphs can be tuned by changing the supersaturation ratio of L-His in aqueous solution, as has been shown in the previous studies.[36,38] When the L-His molecules arrange in the stable polymorph A crystals, they orient imidazole rings in the vicinity of each other, creating a hydrophobic domain within the structure (Figure 2c).

The structure of the L-His crystals therefore features several hydrophobic interior domains while displaying a hydrophilic exterior. To determine whether we could use these hydrophobic domains to entrap small molecules with high entrapment efficiency, we chose three different hydrophobic guest compounds as fluorescent probes (Nile red, pyrene, and β-carotene) and two hydrophilic compounds [fluorescein isothiocyanate (FITC) and norbixin] for comparison. Adding the small molecules individually to aqueous solutions of L-His and subsequently mixing with ethanol, we then collected the resulting L-His crystals after 3 h. X-ray crystallography of the L-His crystals loaded with small molecules showed the change of the crystal's space group from orthorhombic space group $P2_12_12_1$ ($Z = 4$) to the monoclinic space group $P2_1$ ($Z = 2$) in the unit cell (Figure 2d). The transformation from orthorhombic to monoclinic symmetry of His crystals in the presence of hydrophobic small molecules involves minor displacements of atomic positions. As His molecules are crystallized in the presence of hydrophobic small molecules, the intracrystalline voids can be loaded with hydrophobic small molecules, which subsequently alter the hydrogen bonding pattern and electron density of the unit cell. These changes can potentially explain the reason of transformation from orthorhombic to monoclinic symmetry of His crystals in the presence of hydrophobic small molecules.

We also observed the materials using optical microscopy, scanning electron microscopy (SEM), and confocal laser scanning microscopy (CLSM; Figure 3a–d). The hydrophilic small molecules (FITC and norbixin) were not observed entrapped inside the L-His crystals, instead remaining in solution (data not shown). However, fluorescence by the hydrophobic β-carotene, Nile red, and pyrene compounds was observed inside the crystals (Figure 3a–d, iv). These observations demonstrate the entrapment of these molecules in the L-His crystals with entrapment efficiencies of ~96, 62, and 87%, respectively, as determined using high-performance liquid chromatography (HPLC; see the Methods and Materials section). These results indicate that the L-His crystals are specific for the entrapment of hydrophobic small molecules. We believe that the inclusion of such hydrophobic small molecules inside the L-His crystals is noncovalent in nature, driven by hydrophobic interactions, hydrogen bonding, and π–π stacking[39,40] between the imidazole rings of the L-His molecules and the aromatic regions and/or double bonds of the hydrophobic small molecules. The entrapment efficiency may depend on the molecular structure of the small molecules and their ability to fit inside the L-His crystal structure.

The CLSM imaging results of the loaded L-His crystals along the z optical axis (z-stack) indicate that the localization of the hydrophobic small molecules occurs at the central plane of focus (Figure 4, Movies S1 and S2). Figure 4 demonstrates the entrapment of hydrophobic Nile red (Figure 4a,b) and pyrene (Figure 4c) inside the L-His crystals from different dimensional perspectives. Figure 4 verifies that the fluorescent signal of β-carotene (Figure 4d–f) and Nile red (Figure 4g–i) is indeed localized within the structure of the L-His crystals. The entrapment of small molecules inside the fluorescent L-His crystals not only offers the whole system a hydrophilic surface, which can address the challenges of poor solubility and distribution of hydrophobic small molecules in biological systems, but also provides protection and controlled release of the entrapped small molecules.

We also investigated XRD patterns of L-His crystals loaded with different small molecules. Figure 4a illustrates the XRD patterns of pure small molecules (Figure 5a, black lines), pure L-His crystals (Figure 5a, red lines), a dry mixture made of L-His crystals with powders of various small molecules (Figure 5a, blue lines), and small molecule-loaded L-His crystals (Figure 5a, green lines), made as previously described. A characteristic powder diffraction peak of polymorph A appears at $2\theta \approx 19°$ (Figure 5a, red lines). The XRD analysis of crystals obtained from small molecule-loaded L-His crystals (Figure 5a, green lines) yields a different XRD pattern in comparison with the pure L-His crystals (Figure 5a, red lines). The XRD patterns of L-His crystals loaded with β-carotene and Nile red show an increase in the intensity of the peaks at $2\theta \approx 22°$ and 24°, respectively, whereas the XRD pattern of the pyrene-loaded L-His crystals remains similar to that of the pure L-His crystals (Figure 5a, i−iii, green lines). The changes in the peak intensities indicate the change of electron density inside the unit cell and where the atoms are located,[41] and can be influenced by the inclusion of hydrophobic small molecules. This result is in good agreement with the results of single crystal X-ray crystallography, showing the change of the L-His crystals' unit cell upon loading of small molecules (Figure 2c,d). The dominant peaks of the pure small molecules at $2\theta \approx$ 19°, 13°, and 12° for β-carotene, Nile red, and pyrene, respectively (black lines), disappear in the small molecule-loaded crystal samples (green lines), which confirms the loading of the small molecules inside the structure of the L-His crystals. In contrast, for the manual dry mixture of the L-His crystals and small molecules (blue lines), the XRD patterns are different and the dominant peaks of the small molecules at $2\theta \approx$ 19°, 13°, and 12° for β-carotene, Nile red, and pyrene remain (Figure 5a, i−iv).

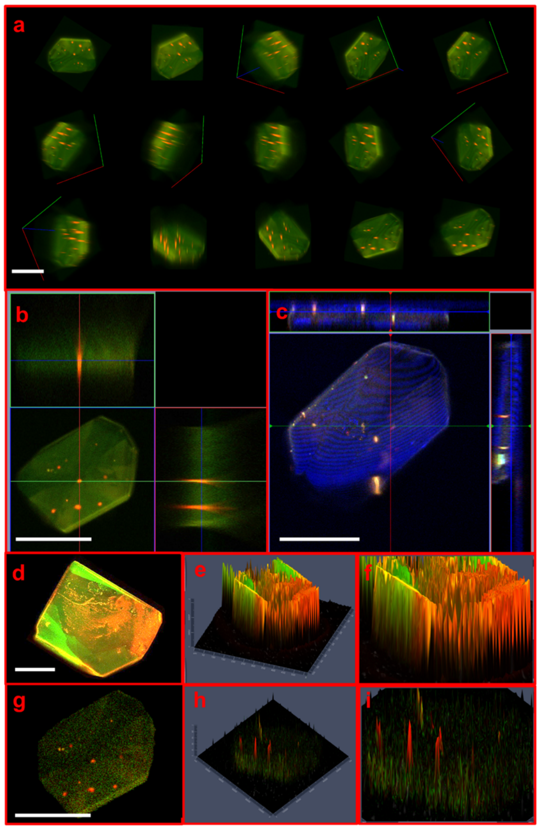

Figure 4. (a) CLSM imaging data collected at different dimensions of the L-His crystals, confirming the localization of the hydrophobic Nile red inside the L-His crystals. (b) Ortho demonstration of L-His crystals with entrapped Nile red. (c) Ortho demonstration of L-His crystals with entrapped pyrene. (d) CLSM imaging data of L-His crystals with entrapped β-carotene in 2D. (e,f) CLSM imaging data of L-His crystals with entrapped β-carotene in 2.5D, with intensity on the Z-axis. (g) L-His crystals with entrapped Nile red in 2D. (h,i) L-His crystals with entrapped Nile red in 2.5D, confirming the localization of the hydrophobic small molecules inside the L-His crystals. The green color represents the L-His crystals, and the orange, blue, and red colors represent the β-carotene, pyrene, and Nile red, respectively. Scale bars: 100 μm.

Because of the exceptional ability of L-His crystals to fluoresce and entrap hydrophobic small molecules within their hydrophilic structure, we applied these crystals to entrap DOX, a highly hydrophobic chemotherapeutic, to address its poor solubility, which can cause cardiotoxicity and lowered systemic bioavailability.[7] Figure 1b shows the L-His crystals loaded with DOX, featuring an entrapment efficiency of 55%. The XRD patterns of the L-His crystals loaded with DOX show an increase in the intensity of the peak at $2\theta \approx 32°$ (green line), indicating that the change of electron density inside the unit cell is potentially influenced by the inclusion of DOX molecules (Figure 5a, iv).

We also demonstrate that the surface of these L-His crystals can be chemically modified to make them site-specific for targeted drug delivery to a specific site of action. Here, we modify the surface of the L-His crystals loaded with DOX using HA (Figure 1c). HA is a natural, nontoxic, and biodegradable acidic polysaccharide composed of *N*-acetylglucosamine and D-glucuronic acid disaccharide units.[42] HA can serve as an active targeting ligand with high binding affinity to cell-membrane-bound CD44 receptors,[26] which are found on the surface of several malignant tumor cells.[43−45] We propose to modify L-His crystals with HA to enhance the specificity of the L-His crystals to deliver DOX to tumor cells and decrease the chance of cytotoxicity and the drug's uptake by normal cells. More importantly, HAase, which plays a significant role in tumor growth, invasion, and metastasis, is widely distributed in the acidic tumor matrix and cleaves internal β-*N*-acetyl-D-glucosamine linkages in the HA.[45] HAase is increased in various malignant tumors, including head and neck, colorectal, brain, prostate, bladder, and metastatic breast cancers.[46] HA binds to the receptor (CD44) on the surface of the cancer cell and is then cleaved by HAase.[46] We hypothesized that this enzyme could be used to hydrolyze HA on the surface of HA-His crystals, allowing the L-His crystals to dissolve in the aqueous matrix and efficiently release the entrapped DOX.

To modify the surface of L-His crystals with HA, we first modified the surface of the L-His crystals with thiolated histidine methyl ester (SH-HME), and then cross-linked the SH-HME with thiolated HA (SH-HA) through the formation of disulfide bonds (Figure 1c, see the Methods and Materials section for more details). Figure S1a shows the schematic illustration for the synthesis of SH-HA and SH-HME. The comparison between Fourier transform infrared (FTIR)

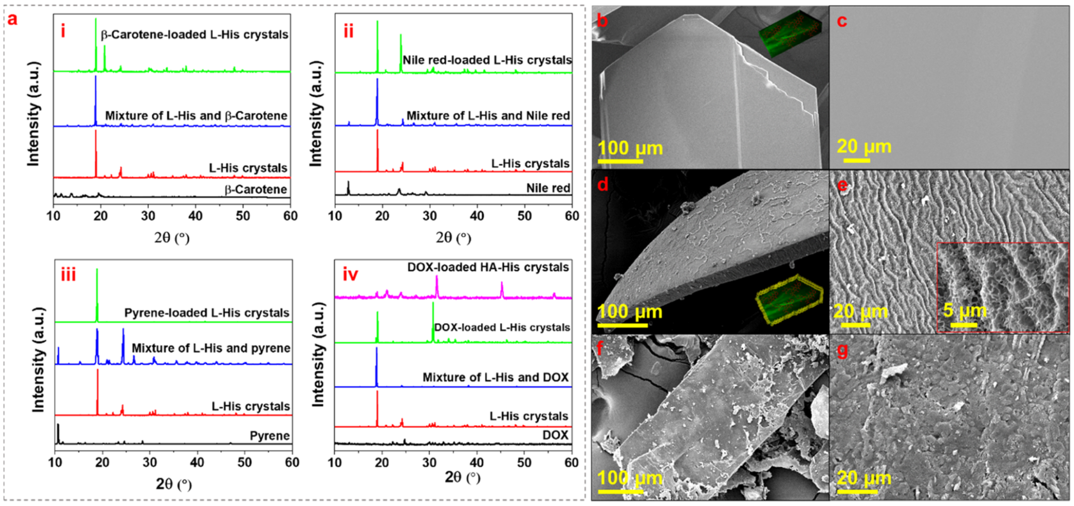

Figure 5. (a) XRD patterns of the L-His crystals with entrapped small molecules (green lines) in comparison with L-His crystals (red lines), small molecules (black lines), a mixture of L-His and small molecules (blue lines), and surface-modified L-His crystals with entrapped small molecules (pink lines) for (i) β-carotene, (ii) Nile red, (iii) pyrene, and (iv) DOX. (b) SEM images of the L-His crystals before surface modification; (c) magnification of (b). (d) L-His crystals after chemical surface modification through disulfide bonds with HA; (e) magnification of (d), with the inset showing a further magnified image. (f) L-His crystals after surface modification through manual mixing of the crystals with HA solution; (g) magnification of (f).

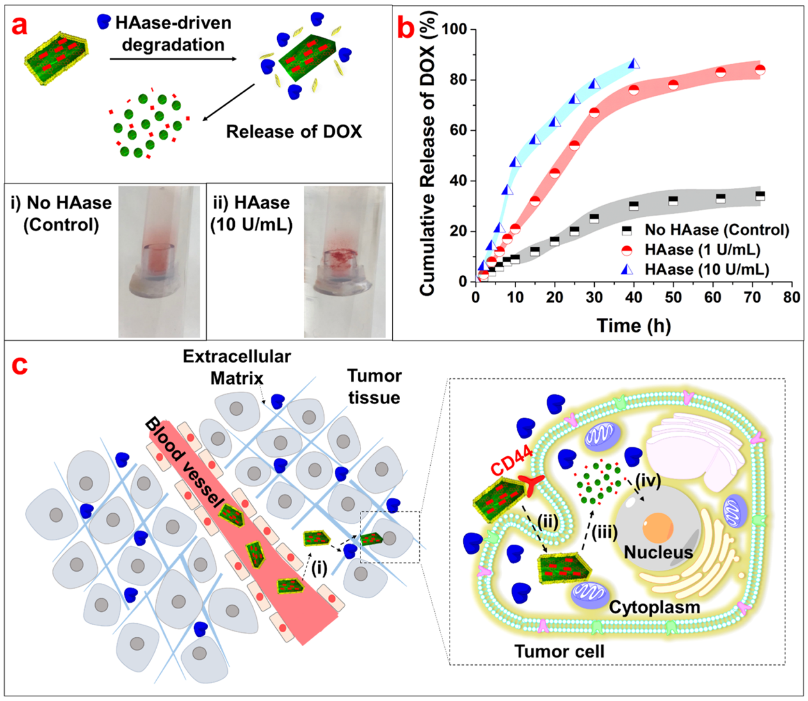

Figure 6. Enzymatic degradation of HA-His crystals in the presence of 1 or 10 U/mL HAase at 37 °C. (a) Schematic of HA-His crystals that can be degraded by HAase, and digital images of the HA-His crystals after 4 h without the presence of HAase [control, (i)] and in the presence of HAase (ii). (b) Cumulative release of DOX from HA-His crystals. (c) Schematic of the enhanced delivery of hydrophobic chemotherapeutics by the HA-His crystals for cancer therapy: (i) HA-His crystals accumulate in the tumor; (ii) HA-His crystals are internalized by the CD44 receptors on the tumor cells; (iii) HAase leads to the degradation of HA on the crystal surface, dissolving the crystals; and (iv) release of the hydrophobic chemotherapeutics over time to cause the tumor cell death.

spectra of HA and SH-HA shows a significant decrease of the peak at 1610−1620 cm^{-1} associated with the HA carboxyl groups, confirming the formation of SH-HA (Figure S1b). Figure S1c shows the formation of disulfide bonds between SH-HA and SH-HME. The L-His crystals are smooth before surface modification (SEM images, Figure 5b,c). The chemical modification of the L-His crystals through the formation of disulfide bonds between SH-HME and SH-HA forms a uniform layer of HA on the surface of the L-His crystals (Figure 5d,e). In contrast, applying the HA solution directly to the surface of the L-His crystals does not result in a uniform layer on the crystal (Figure 5f,g). Surface modification of the L-His crystals with HA also changes the XRD pattern, showing two dominant peaks at $2\theta \approx 33°$ and 46° (Figure 5a, iv, pink line).

We compared the release behaviors of DOX from the HA-His crystals after incubation with and without HAase (Figure 6a,b). Figure 6a illustrates that the HA-His crystals start to disintegrate in the presence of HAase after 4 h. In vitro release experiments revealed that less than 35% of DOX is released from the HA-His crystals after 72 h in a phosphate buffer, whereas 84% of DOX is released during that same time in the presence of 1 U/mL HAase (Figure 6b). In the presence of 10 U/mL HAase, the release rate is accelerated and 86% of DOX is released in 40 h (Figure 6b). This result indicates that the HA-His crystals incubated with HAase markedly increase the release of DOX. Thus, HA-His crystals can potentially bind to CD44 receptors on the surface of tumor cells, enhancing the cellular uptake, and then release entrapped DOX upon degradation by HAase to the intracellular compartments of tumors, increasing apoptosis of tumor cells (Figure 6c).

CONCLUSIONS

In this work, we demonstrate the entrapment of hydrophobic small molecules inside the hydrophobic domains of L-His crystals, providing a potential biocompatible platform for protecting hydrophobic drugs. As the entrapment of hydrophobic small molecules is at the molecular level, the entrapment efficiency is relatively high and possibly depends on the molecular structure of the small molecules. We confirm the entrapment of hydrophobic small molecules inside the L-His crystals using confocal microscopy. Moreover, the X-ray powder diffraction and single crystals X-ray crystallography data show the change of electron density and symmetry in L-His crystals. Interestingly, we demonstrate that the symmetry of L-His crystals is changed from orthorhombic to monoclinic in the presence of the hydrophobic small molecules. This change can be due to the change in the hydrogen-bonding pattern between L-His molecules in the presence of hydrophobic small molecules. The modification of the L-His crystals at the surface using polymers and/or hydrogels could enable intracellular trafficking and site-specific delivery of hydrophobic therapeutics, providing a drug-delivery system with targeting features. For example, the L-His crystals with HA covalently bonded to their surface and loaded with DOX are able to target tumor cells and control the release of DOX in response to HAase overexpressed in these cells. We demonstrate that the HAase can increase the rate of DOX release from the HA-His crystals. The composition of the surface can be controlled and tuned for optimization with other enzymes and physiological media. Releasing the entrapped hydrophobic drugs as the HA-His crystals are degraded and dissolved in the aqueous media can also reduce the chance of local toxicity to normal cells due to drug aggregation. The successful entrapment and targeted release of hydrophobic small molecules in the HA-His crystals suggests that further study is warranted to probe the possible implementation of amino acid crystals in promoting the delivery of hydrophobic therapeutics with low solubility and/or delivery of a combination of hydrophobic drugs to treat multidrug resistance. This strategy helps to address issues related to the poor solubility and low bioavailability of such molecules. These L-His crystals can also be investigated in terms of improving the imaging and tracking of entrapped therapeutic agents due to the crystals' natural fluorescence properties. However, further research and in vivo studies are essential before the potential of HA-His crystals in cancer therapy can become a reality.

METHODS AND MATERIALS

Preparation and Characterization of the L-His Crystals with Entrapped Small Molecules. A 30 mg/mL solution of L-His (≥99%, Sigma-Aldrich) was prepared by dissolving L-His powder in Milli-Q water using a vortex mixer at ambient temperature in a Corning 15 mL centrifuge tube with a closed cap. Then, 500 μL of the aqueous solution of L-His and 500 μL of 200 proof ethanol (KOPTEC, PA, US) were added to 200 μL of the small molecule solution (2 mg/mL). The small molecules used in this study were Nile red (>98%, Sigma-Aldrich), pyrene (>98%, Sigma-Aldrich), β-carotene (>97%, Sigma-Aldrich), and DOX HCl (DOX, >98%, Fluka, Mexico City, Mexico). The solution was vortexed for 15 s and kept static at ambient temperature. After 3 h, crystals were collected and washed with ethanol to remove the free small molecules from the surface of the crystals and the supernatant was collected to measure the concentration of the nonentrapped small molecules using HPLC. An Agilent 1200 LC System with a binary SL pump & diode array detector, Shodex RI-501 refractive index detector (single channel) and an Agilent 1100 column compartment (G1316) was utilized to carry out the analysis. Each individual sample of small molecules was quantified based on an optimized method reported in the literature for β-carotene,[47] Nile red,[48] pyrene,[49] and DOX.[50] The entrapment efficiency of the crystals was calculated by subtracting the concentration of the nonentrapped small molecules in the supernatant from the primary amount of small molecules, as follows in eq 1

$$\text{Entrapment efficiency (\%)} = \frac{M_0 - M_s}{M_0} \times 100 \tag{1}$$

in which M_0 is the primary concentration of small molecules used in the formulation, and M_s is the concentration of nonentrapped small molecules in the supernatant.

L-His crystal controls were prepared using the same procedure, but without the addition of small molecules. Unit cell data for the L-His crystals were collected on a Rigaku Synergy XtaLAB diffractometer. The morphologies of the crystals were observed using a Zeiss 710 laser scanning confocal microscope (Carl Zeiss Microscopy, Thornwood, NY), an inverted optical microscope (DMIL LED, Leica) connected to a fast camera (MicroLab 3a10, Vision Research), and a scanning electron microscope (LEO Zeiss 1550 FESEM (Keck SEM) and Zeiss Gemini 500). All SEM images were obtained under the high vacuum mode without sputter coating. XRD measurements were performed using a Bruker D8 ADVANCE ECO powder diffractometer (MA) operated at 40 kV and 30 mA (Cu Kα radiation). The crystals were scanned at room temperature from 2θ = 10−60° under continuous scanning in 0.02 steps of 2θ min^{-1}.

Synthesis of Thiolated HA. Sodium hyaluronate (>43% glucuronic acid, Bulk Supplements, Henderson, NV, USA) was used after being dialyzed against distilled water, followed by lyophilization. L-cysteine methyl ester was synthesized to protect the carboxyl groups of L-cysteine using a previously described method.[51] The covalent attachment of L-cysteine methyl ester to sodium hyaluronate was achieved through the formation of amide bonds between the primary amino groups of the cysteine methyl ester and the carboxylic groups of hyaluronate. To synthesize SH-HA, we used a method previously reported in the literature.[52] In brief, sodium hyaluronate (2.5 mmol) was dissolved in 100 mL of distilled water, to which *N*-(3-dimethylaminopropyl)-*N*′-ethylcarbodiimide hydrochloride (0.5 mmol, >98%, Sigma-Aldrich) and cysteine methyl ester (2.5 mmol) were added under slow stirring. The pH was adjusted to 5.3 by the addition of 1 M NaOH. After incubating the solution for 5 h, the solution was transferred to dialysis membrane discs (MWCO 3.5 kDa, Thermo Scientific) and dialyzed three times against 1% NaCl for 3 days, and finally against distilled water for 1 day. The solutions were then freeze-dried to obtain a white solid and investigated by FTIR in the region from 4000 to 400 cm^{-1} (120 scans, resolution of 2 cm^{-1}) using an IRAffinity-1S FTIR spectrophotometer (Shimadzu Scientific Instruments/Marlborough, MA).

Synthesis of Thiolated Histidine Methyl Ester. Histidine methyl ester (HME) was synthesized using a previously described method.[51] The SH-HME was synthesized by reacting HME (1 mmol) with 2-iminothiolane hydrochloride (0.4 mmol, >98%, Sigma-Aldrich) in PBS (50 mL; pH 7.4) for 12 h at room temperature. After washing the SH-HME using deionized water, the solution was lyophilized to obtain a powder of SH-HME.

Synthesis of HAase-Responsive, HA-Modified Histidine Crystals with Entrapped DOX (HA-His Crystals). After synthesizing the L-His crystals with entrapped DOX, as described earlier, SH-HME (0.01 g) was added to the crystal dispersion, followed by the addition of 200 μL of ethanol to start growing the SH-HME crystals on the surface of the L-His crystals to form thiolated histidine crystals (SH-His crystals). The SH-His crystals were incubated at room temperature for 3 h. Next, SH-HA (0.03 g) was added to the SH-His crystal dispersion, and the pH was adjusted to 8 with 1 M NaOH. Then, 50 μL of chloramine T solution (50 mM in PBS buffer, pH 7.4, >98%, Sigma-Aldrich) was added, based on a previously reported method,[53] to induce thiol-mediated conjugation of the SH-HA onto the SH-His crystals. After 1 h incubation at room temperature, the resulting HA-modified histidine crystals (HA-His crystals) were collected from the falcon tubes by centrifugation at 1000*g* for 5 min, washed with ethanol, freeze-dried, and stored at 4 °C.

In Vitro Enzyme-Triggered Drug Release of DOX-Loaded HA-His Crystals. HAase-triggered drug release profiles of the DOX-loaded HA-His crystals were monitored using HPLC. The DOX-loaded HA-His crystals were incubated with different concentrations of HAase in an acetate buffer (pH = 4.3, 37 °C) for 72 h. To measure the drug release profiles of DOX, we used HPLC and attained the data at predetermined time points after incubating the DOX-loaded HA-His crystals with the acetate buffer. Supernatants were used to measure the drug release profiles using a dialysis method. In brief, lyophilized HA-His crystals (5 mg) were dispersed in 1 mL of acetate buffer (pH = 4.3, 37 °C) containing different concentrations of HAase (0, 1, and 10 U/mL). The dispersed HA-His crystals were transferred to Spectra/Por regenerated cellulose dialysis tubes (molecular weight cutoff = 10 000, Float A lyzer) immersed in 15 mL of acetate buffer (pH = 4.3, 37 °C) containing 1.6% Triton X-100 and gently shaken at 37 °C in a water bath at 100 rpm. The medium was replaced with fresh medium at predetermined time points. The cumulative release of DOX was calculated as per eq 2

$$\text{Cumulative release (\%)} = (M_t/M_\infty) \times 100 \qquad (2)$$

in which M_t is the amount of DOX released from the crystals at time t, and M_∞ is the amount of DOX in the crystals.

Statistical Analysis. The results were subjected to analysis of variance (ANOVA) using SPSS software package version 15.0 for Windows. All measurements were performed in triplicate. Mean comparisons were performed using the post hoc multiple comparison Duncan test to determine if differences were significant at $P < 0.05$.

■ ASSOCIATED CONTENT

Supporting Information

The Supporting Information is available free of charge on the ACS Publications website at DOI: 10.1021/acsami.9b14239.

Schematic illustration for the synthesis of SH-HA and SH-HME (PDF)

Entrapment of hydrophobic small molecules inside L-His crystals from different dimensions (MP4)

CLSM imaging results of L-His crystals loaded with hydrophobic small molecules (MP4)

■ AUTHOR INFORMATION

Corresponding Author

*E-mail: alireza@cornell.edu.

ORCID

Alireza Abbaspourrad: 0000-0001-5617-9220

Notes

The authors declare no competing financial interest.

■ ACKNOWLEDGMENTS

The authors thank Peter Lawrence and Carol J. Bayles. This work is supported by Cornell Technology Acceleration and Maturation (CTAM) fund award number G488711, the Cornell Center for Materials Research (CCMR), the Biotechnology Resource Center (BRC) at Cornell University and instrumentation grant NIH S10RR025502 for the Zeiss LSM 710 Confocal. This work made use of the Cornell Center for Materials Research Facilities supported by the National Science Foundation under Award Number DMR-1719875.

■ REFERENCES

(1) Liu, Z.; Robinson, J. T.; Sun, X.; Dai, H. PEGylated Nanographene Oxide for Delivery of Water-insoluble Cancer Drugs. *J. Am. Chem. Soc.* **2008**, *130*, 10876−10877.

(2) Lipinski, C. A.; Lombardo, F.; Dominy, B. W.; Feeney, P. J. Experimental and Computational Approaches to Estimate Solubility and Permeability in Drug Discovery and Development Settings. *Adv. Drug Delivery Rev.* **2012**, *64*, 4−17.

(3) Fernandez, A.-M.; Van derpoorten, K.; Dasnois, L.; Lebtahi, K.; Dubois, V.; Lobl, T. J.; Gangwar, S.; Oliyai, C.; Lewis, E. R.; Shochat, D.; Trouet, A. N-Succinyl-(β-Alanyl-L-Leucyl-L-Alanyl-L-Leucyl) Doxorubicin: An Extracellularly Tumor-activated Prodrug Devoid of Intravenous Acute Toxicity. *J. Med. Chem.* **2001**, *44*, 3750−3753.

(4) Allen, T. M.; Cullis, P. R. Drug Delivery Systems: Entering the Mainstream. *Science* **2004**, *303*, 1818−1822.

(5) Fritze, A.; Hens, F.; Kimpfler, A.; Schubert, R.; Peschka-Süss, R. Remote Loading of Doxorubicin into Liposomes Driven by a Transmembrane Phosphate Gradient. *Biochim. Biophys. Acta, Biomembr.* **2006**, *1758*, 1633−1640.

(6) Wang, S.; Konorev, E. A.; Kotamraju, S.; Joseph, J.; Kalivendi, S.; Kalyanaraman, B. Doxorubicin Induces Apoptosis in Normal and Tumor Cells via Distinctly Different Mechanisms Intermediacy of H2O2-and p53-Dependent Pathways. *J. Biol. Chem.* **2004**, *279*, 25535−25543.

(7) Torchilin, V. P. Targeted Polymeric Micelles for Delivery of Poorly Soluble Drugs. *Cell. Mol. Life Sci.* **2004**, *61*, 2549−2559.

(8) Kim, C. K.; Ghosh, P.; Pagliuca, C.; Zhu, Z.-J.; Menichetti, S.; Rotello, V. M. Entrapment of Hydrophobic Drugs in Nanoparticle Monolayers with Efficient Release into Cancer Cells. *J. Am. Chem. Soc.* **2009**, *131*, 1360−1361.

(9) Ravanfar, R.; Tamaddon, A. M.; Niakousari, M.; Moein, M. R. Preservation of Anthocyanins in Solid Lipid Nanoparticles: Optimization of a Microemulsion Dilution Method Using the Placket−Burman and Box−Behnken Designs. *Food Chem.* **2016**, *199*, 573−580.

(10) Ravanfar, R.; Comunian, T. A.; Dando, R.; Abbaspourrad, A. Optimization of Microcapsules Shell Structure to Preserve Labile Compounds: A Comparison between Microfluidics and Conventional Homogenization Method. *Food Chem.* **2018**, *241*, 460−467.

(11) Ravanfar, R.; Comunian, T. A.; Abbaspourrad, A. Thermoresponsive, Water-dispersible Microcapsules with a Lipid-polysaccharide Shell to Protect Heat-sensitive Colorants. *Food Hydrocolloids* **2018**, *81*, 419.

(12) Mehrad, B.; Ravanfar, R.; Licker, J.; Regenstein, J. M.; Abbaspourrad, A. Enhancing the Physicochemical Stability of β-Carotene Solid Lipid Nanoparticle (SLNP) Using Whey Protein Isolate. *Food Res. Int.* **2018**, *105*, 962−969.

(13) Comunian, T. A.; Ravanfar, R.; Selig, M. J.; Abbaspourrad, A. Influence of the Protein Type on the Stability of Fish Oil in Water Emulsion Obtained by Glass Microfluidic Device. *Food Hydrocolloids* **2017**, *77*, 96.

(14) Comunian, T. A.; Ravanfar, R.; de Castro, I. A.; Dando, R.; Favaro-Trindade, C. S.; Abbaspourrad, A. Improving Oxidative

Stability of Echium Oil Emulsions Fabricated by Microfluidics: Effect of Ionic Gelation and Phenolic Compounds. *Food Chem.* **2017**, *233*, 125−134.

(15) Cho, K.; Wang, X.; Nie, S.; Chen, Z.; Shin, D. M. Therapeutic Nanoparticles for Drug Delivery in Cancer. *Clin. Cancer Res.* **2008**, *14*, 1310−1316.

(16) Lu, J.; Liong, M.; Zink, J. I.; Tamanoi, F. Mesoporous Silica Nanoparticles as a Delivery System for Hydrophobic Anticancer Drugs. *Small* **2007**, *3*, 1341−1346.

(17) Allen, T. M.; Cullis, P. R. Liposomal Drug Delivery Systems: from Concept to Clinical Applications. *Adv. Drug Delivery Rev.* **2013**, *65*, 36−48.

(18) Hoffman, A. S. Stimuli-responsive Polymers: Biomedical Applications and Challenges for Clinical Translation. *Adv. Drug Delivery Rev.* **2013**, *65*, 10−16.

(19) Ravanfar, R.; Celli, G. B.; Abbaspourrad, A. Controlling the Release from Enzyme-responsive Microcapsules with a Smart Natural Shell. *ACS Appl. Mater. Interfaces* **2018**, *10*, 6046−6053.

(20) Zhan, S.; Wang, J.; Wang, W.; Cui, L.; Zhao, Q. Preparation and In Vitro Release Kinetics of Nitrendipine-loaded PLLA−PEG−PLLA Microparticles by Supercritical Solution Impregnation Process. *RSC Adv.* **2019**, *9*, 16167−16175.

(21) Ghorpade, V. S.; Yadav, A. V.; Dias, R. J.; Mali, K. K.; Pargaonkar, S. S.; Shinde, P. V.; Dhane, N. S. Citric Acid Crosslinked Carboxymethylcellulose-poly (ethylene glycol) Hydrogel Films for Delivery of Poorly Soluble Drugs. *Int. J. Biol. Macromol.* **2018**, *118*, 783−791.

(22) Upponi, J. R.; Jerajani, K.; Nagesha, D. K.; Kulkarni, P.; Sridhar, S.; Ferris, C.; Torchilin, V. P. Polymeric Micelles: Theranostic Co-delivery System for Poorly Water-soluble Drugs and Contrast Agents. *Biomaterials* **2018**, *170*, 26−36.

(23) Chen, L.; Remondetto, G.; Rouabhia, M.; Subirade, M. Kinetics of the Breakdown of Cross-linked Soy Protein Films for Drug Delivery. *Biomaterials* **2008**, *29*, 3750−3756.

(24) Elzoghby, A. O.; Samy, W. M.; Elgindy, N. A. Protein-based Nanocarriers as Promising Drug and Gene Delivery Systems. *J. Controlled Release* **2012**, *161*, 38−49.

(25) Comunian, T. A.; Ravanfar, R.; Alcaine, S. D.; Abbaspourrad, A. Water-in-oil-in-water Emulsion Obtained by Glass Microfluidic Device for Protection and Heat-triggered Release of Natural Pigments. *Food Res. Int.* **2018**, *106*, 945−951.

(26) Zhu, Q.; Chen, X.; Xu, X.; Zhang, Y.; Zhang, C.; Mo, R. Tumor-Specific Self-Degradable Nanogels as Potential Carriers for Systemic Delivery of Anticancer Proteins. *Adv. Funct. Mater.* **2018**, *28*, 1707371.

(27) Maiti, C.; Parida, S.; Kayal, S.; Maiti, S.; Mandal, M.; Dhara, D. Redox-responsive Core-cross-linked Block Copolymer Micelles for Overcoming Multidrug Resistance in Cancer Cells. *ACS Appl. Mater. Interfaces* **2018**, *10*, 5318−5330.

(28) Miatmoko, A.; Kawano, K.; Yonemochi, E.; Hattori, Y. Evaluation of Cisplatin-Loaded Polymeric Micelles and Hybrid Nanoparticles Containing Poly (Ethylene Oxide)-Block-Poly (Methacrylic Acid) on Tumor Delivery. *Pharmacol. Pharm.* **2016**, *07*, 1.

(29) Morgan, M. T.; Nakanishi, Y.; Kroll, D. J.; Griset, A. P.; Carnahan, M. A.; Wathier, M.; Oberlies, N. H.; Manikumar, G.; Wani, M. C.; Grinstaff, M. W. Dendrimer-encapsulated Camptothecins: Increased Solubility, Cellular Uptake, and Cellular Retention Affords Enhanced Anticancer Activity In Vitro. *Cancer Res.* **2006**, *66*, 11913−11921.

(30) Li, Z.; Chen, Q.; Qi, Y.; Liu, Z.; Hao, T.; Sun, X.; Qiao, M.; Ma, X.; Xu, T.; Zhao, X.; Yang, C.; Chen, D. Rational Design of Multifunctional Polymeric Nanoparticles Based on Poly(l-histidine) and d-α-Vitamin E Succinate for Reversing Tumor Multidrug Resistance. *Biomacromolecules* **2018**, *19*, 2595−2609.

(31) Lee, S.-J.; Jeong, Y.-I. Hybrid Nanoparticles Based on Chlorin e6-conjugated Hyaluronic Acid/Poly (l-histidine) Copolymer for Theranostic Application to Tumors. *J. Mater. Chem. B* **2018**, *6*, 2851−2859.

(32) Jia, L.; Jia, N.; Gao, Y.; Hu, H.; Zhao, X.; Chen, D.; Qiao, M. Multi-Modulation of Doxorubicin Resistance in Breast Cancer Cells by Poly (l-histidine)-Based Multifunctional Micelles. *Pharmaceutics* **2019**, *11*, 385.

(33) Warżajtis, B.; Glišić, B. Đ.; Savić, N. D.; Pavic, A.; Vojnovic, S.; Veselinović, A.; Nikodinovic-Runic, J.; Rychlewska, U.; Djuran, M. I. Mononuclear Gold (III) Complexes with L-Histidine-containing Dipeptides: Tuning the Structural and Biological Properties by Variation of the N-terminal Amino Acid and Counter Anion. *Dalton Trans.* **2017**, *46*, 2594−2608.

(34) Preimesberger, M. R.; Majumdar, A.; Rice, S. L.; Que, L.; Lecomte, J. T. J. Helix-Capping Histidines: Diversity of N−H··· N Hydrogen Bond Strength Revealed by 2h J NN Scalar Couplings. *Biochemistry* **2015**, *54*, 6896−6908.

(35) Li, S.; Hong, M. Protonation, Tautomerization, and Rotameric Structure of Histidine: A Comprehensive Study by Magic-angle-spinning Solid-state NMR. *J. Am. Chem. Soc.* **2011**, *133*, 1534−1544.

(36) Roelands, C. P. M.; Jiang, S.; Kitamura, M.; ter Horst, J. H.; Kramer, H. J. M.; Jansens, P. J. Antisolvent Crystallization of the Polymorphs of L-Histidine as a Function of Supersaturation Ratio and of Solvent Composition. *Cryst. Growth Des.* **2006**, *6*, 955−963.

(37) Madden, J. J.; McGandy, E. L.; Seeman, N. C. The Crystal Structure of the Orthorhombic Form of L-(+)-Histidine. *Acta Crystallogr., Sect. B: Struct. Crystallogr. Cryst. Chem.* **1972**, *28*, 2377−2382.

(38) Wantha, L.; Punmalee, N.; Sawaddiphol, V.; Flood, A. E. Effect of Ethanol on Crystallization of the Polymorphs of L-Histidine. *J. Cryst. Growth* **2018**, *490*, 65−70.

(39) Chen, R. J.; Zhang, Y.; Wang, D.; Dai, H. Noncovalent Sidewall Functionalization of Single-walled Carbon Nanotubes for Protein Immobilization. *J. Am. Chem. Soc.* **2001**, *123*, 3838−3839.

(40) Liu, Z.; Sun, X.; Nakayama-Ratchford, N.; Dai, H. Supramolecular Chemistry on Water-soluble Carbon Nanotubes for Drug Loading and Delivery. *ACS Nano* **2007**, *1*, 50−56.

(41) Guo, W.; Liu, J.; Weidler, P. G.; Liu, J.; Neumann, T.; Danilov, D.; Wenzel, W.; Feldmann, C.; Wöll, C. Loading of Ionic Compounds into Metal−organic Frameworks: A Joint Theoretical and Experimental Study for the Case of La 3+. *Phys. Chem. Chem. Phys.* **2014**, *16*, 17918−17923.

(42) Lee, M.-Y.; Park, S.-J.; Park, K.; Kim, K. S.; Lee, H.; Hahn, S. K. Target-specific Gene Silencing of Layer-by-layer Assembled Gold−cysteamine/siRNA/PEI/HA Nanocomplex. *ACS Nano* **2011**, *5*, 6138−6147.

(43) Wang, L.; Su, W.; Liu, Z.; Zhou, M.; Chen, S.; Chen, Y.; Lu, D.; Liu, Y.; Fan, Y.; Zheng, Y.; Han, Z.; Kong, D.; Wu, J. C.; Xiang, R.; Li, Z. CD44 Antibody-targeted Liposomal Nanoparticles for Molecular Imaging and Therapy of Hepatocellular Carcinoma. *Biomaterials* **2012**, *33*, 5107−5114.

(44) Li, J.; Huo, M.; Wang, J.; Zhou, J.; Mohammad, J. M.; Zhang, Y.; Zhu, Q.; Waddad, A. Y.; Zhang, Q. Redox-sensitive Micelles Self-assembled from Amphiphilic Hyaluronic Acid-deoxycholic Acid Conjugates for Targeted Intracellular Delivery of Paclitaxel. *Biomaterials* **2012**, *33*, 2310−2320.

(45) Jiang, T.; Zhang, Z.; Zhang, Y.; Lv, H.; Zhou, J.; Li, C.; Hou, L.; Zhang, Q. Dual-functional Liposomes Based on pH-responsive Cell-penetrating Peptide and Hyaluronic Acid for Tumor-targeted Anticancer Drug Delivery. *Biomaterials* **2012**, *33*, 9246−9258.

(46) Choi, K. Y.; Yoon, H. Y.; Kim, J.-H.; Bae, S. M.; Park, R.-W.; Kang, Y. M.; Kim, I.-S.; Kwon, I. C.; Choi, K.; Jeong, S. Y.; Kim, K.; Park, J. H. Smart Nanocarrier Based on PEGylated Hyaluronic Acid for Cancer Therapy. *ACS Nano* **2011**, *5*, 8591−8599.

(47) Etzbach, L.; Pfeiffer, A.; Weber, F.; Schieber, A. Characterization of Carotenoid Profiles in Goldenberry (Physalis peruviana L.) Fruits at Various Ripening Stages and in Different Plant Tissues by HPLC-DAD-APCI-MSn. *Food Chem.* **2018**, *245*, 508−517.

(48) Wu, X.; Biatry, B.; Cazeneuve, C.; Guy, R. H. Drug Delivery to the Skin from Sub-micron Polymeric Particle Formulations: Influence of Particle Size and Polymer Hydrophobicity. *Pharm. Res.* **2009**, *26*, 1995−2001.

(49) Jia, H.; Hou, D.; Dai, M.; Lu, H.; Yan, C. Effects of Root Exudates on the Mobility of Pyrene in Mangrove Sediment-water System. *Catena* **2018**, *162*, 396−401.

(50) Chi, Y.; Yin, X.; Sun, K.; Feng, S.; Liu, J.; Chen, D.; Guo, C.; Wu, Z. Redox-sensitive and Hyaluronic Acid Functionalized Liposomes for Cytoplasmic Drug Delivery to Osteosarcoma in Animal Models. *J. Controlled Release* **2017**, *261*, 113−125.

(51) Hosangadi, B. D.; Dave, R. H. An Efficient General Method for Esterification of Aromatic Carboxylic Acids. *Tetrahedron Lett.* **1996**, *37*, 6375−6378.

(52) Ouasti, S.; Donno, R.; Cellesi, F.; Sherratt, M. J.; Terenghi, G.; Tirelli, N. Network Connectivity, Mechanical Properties and Cell Adhesion for Hyaluronic Acid/PEG Hydrogels. *Biomaterials* **2011**, *32*, 6456−6470.

(53) Fan, Y.; Sahdev, P.; Ochyl, L. J.; Akerberg, J.; Moon, J. J. Cationic Liposome−hyaluronic Acid Hybrid Nanoparticles for Intranasal Vaccination with Subunit Antigens. *J. Controlled Release* **2015**, *208*, 121−129.